Dalton Transactions

ROYAL SOCIETY OF CHEMISTRY

PAPER

View Article Online
View Journal | View Issue



Check for updates

Cite this: *Dalton Trans.*, 2022, **51**, 4297

# Heteroleptic *mer*-[Cr(N^N^N)(CN)$_3$] complexes: synthetic challenge, structural characterization and photophysical properties†

Julien Chong,[a] Céline Besnard,[b] Carlos M. Cruz,[c] Claude Piguet *[a] and Juan-Ramón Jiménez *[a,d]

Received 14th January 2022,
Accepted 17th February 2022

DOI: 10.1039/d2dt00126h

rsc.li/dalton

The substitution of three water molecules around trivalent chromium in $CrBr_3 \cdot 6H_2O$ with the tridentate 2,2′:6′,2″-terpyridine (tpy), *N*,*N*′-dimethyl-*N*,*N*′-di(pyridine-2-yl)pyridine-2,6-diamine (ddpd) or 2,6-di(quinolin-8-yl)pyridine (dqp) ligands gives the heteroleptic *mer*-[Cr(**L**)$Br_3$] complexes. Stepwise treatments with $Ag(CF_3SO_3)$ and KCN under microwave irradiations provide *mer*-[Cr(**L**)$(CN)_3$] in moderate yields. According to their X-ray crystal structures, the associated six-coordinate meridional $[CrN_3C_3]$ chromophores increasingly deviate from a pseudo-octahedral arrangement according to L = ddpd ≈ dpq ≪ tpy; a trend in line with the replacement of six-membered with five-membered chelate rings around $Cr^{III}$. Room-temperature ligand-centered UV-excitation at 18 170 $cm^{-1}$ ($\lambda_{exc}$ = 350 nm), followed by energy transfer and intersystem crossing eventually yield microsecond metal-centered $Cr(^2E \rightarrow {}^4A_2)$ phosphorescence in the red to near infrared domain 13 150–12 650 $cm^{-1}$ (760 ≤ $\lambda_{em}$ ≤ 790 nm). Decreasing the temperature to liquid nitrogen (77 K) extends the emission lifetimes to reach the millisecond regime with a record of 4.02 ms for *mer*-[Cr(dqp)$(CN)_3$] in frozen acetonitrile.

## Introduction

The $[Ar]3d^3$ electronic configuration found in pseudo-octahedral trivalent chromium complexes is famous for its orbitally non-degenerate paramagnetic $^4A_2$ ground state, which is ideally suited (i) for maximizing kinetic inertness with respect to ligand exchange reactions,[1] a prerequisite for the design of heteroleptic complexes,[2] and (ii) for programming magnetic exchange interactions with adjacent open-shell partners[3] as found, for instance, in ferromagnetic Prussian blue-like $Cs^INi^{II}[Cr^{III}(CN)_6] \cdot 2H_2O$[4] or $Na^IMn^{II}[Cr^{III}(CN)_6] \cdot 2H_2O$[5] phases. Moreover, the energy of the metal-centered excited states $Cr(^2E)$, $Cr(^2T_1)$ and $Cr(^4T_2)$, which control the optical properties, can be easily tuned by the primary coordination sphere around the chromium center *via* the ligand field ($\Delta$) and Racah ($B$, $C$) parameters (Scheme 1 and Table S1†).[6–13] Whereas the design of inert heteroleptic trivalent chromium complexes has been systematically exploited within the frame of the 'complex-as-ligand and complex-as-metal' strategy for producing heteropolymetallic paramagnetic assemblies and clusters working as ferromagnets or single-molecule magnets (SMMs),[3,14–19] the alternative building of optical devices using the same strategy remained scarce.[20–23] Under weak ligand field conditions, as found in $[CrX_6]^{3-}$ (X = F, Cl) and in $[CrO_6]$ chromophores possessing $\Delta/B$ < 30 (Scheme 1a, Table S1†), the excited $Cr(^4T_2)$ and $Cr(^2E,{}^2T_1)$ levels are close in energy and involved in back-intersystem crossing (BISC) processes.[24–29] These circumstances produce: (i) $Cr(^4T_2 \rightarrow {}^4A_2)$ fluorescence (green arrow in Scheme 1b) and (ii) $Cr(^2T_1,{}^2E \rightarrow {}^4A_2)$ phosphorescence (red arrows in Scheme 1b) with short excited-state lifetimes.[2,11] The situation changes for strong field $[CrN_6]$ and $[CrC_6]$ chromophores with $\Delta/B$ > 30 (Scheme 1a) because (i) the large energy gap $\Delta E = E(^4T_2) - E(^2T_1,{}^2E)$ prevents BISC and (ii) the intersystem crossing $Cr(^4T_2 \rightarrow {}^2T_1,{}^2E)$ process is fast.[30,31] This ensures an efficient feeding of the long-lived doublet $Cr(^2T_1,{}^2E)$ excited states (Scheme 1b) and phosphorescence dominates the emission process. Competition between phosphorescence and intermetallic energy transfers thus becomes accessible in d–f

[a]*Department of Inorganic and Analytical Chemistry, University of Geneva, 30 quai E. Ansermet, CH-1211 Geneva 4, Switzerland. E-mail: Claude.Piguet@unige.ch*
[b]*Laboratory of Crystallography, University of Geneva, 24 quai E. Ansermet, CH-1211 Geneva 4, Switzerland*
[c]*Department of Chemistry, University of Zurich, Winterthurerstrasse 190, CH-8057 Zurich, Switzerland*
[d]*Department of Inorganic Chemistry, University of Granada and "Unidad de Excelencia en Química" (UEQ), Avda. Fuentenueva, E-18071 Granada, España. E-mail: jrjimenez@ugr.es*

†Electronic supplementary information (ESI) available. CCDC 2133575–2133578. For ESI and crystallographic data in CIF or other electronic format see DOI: 10.1039/d2dt00126h

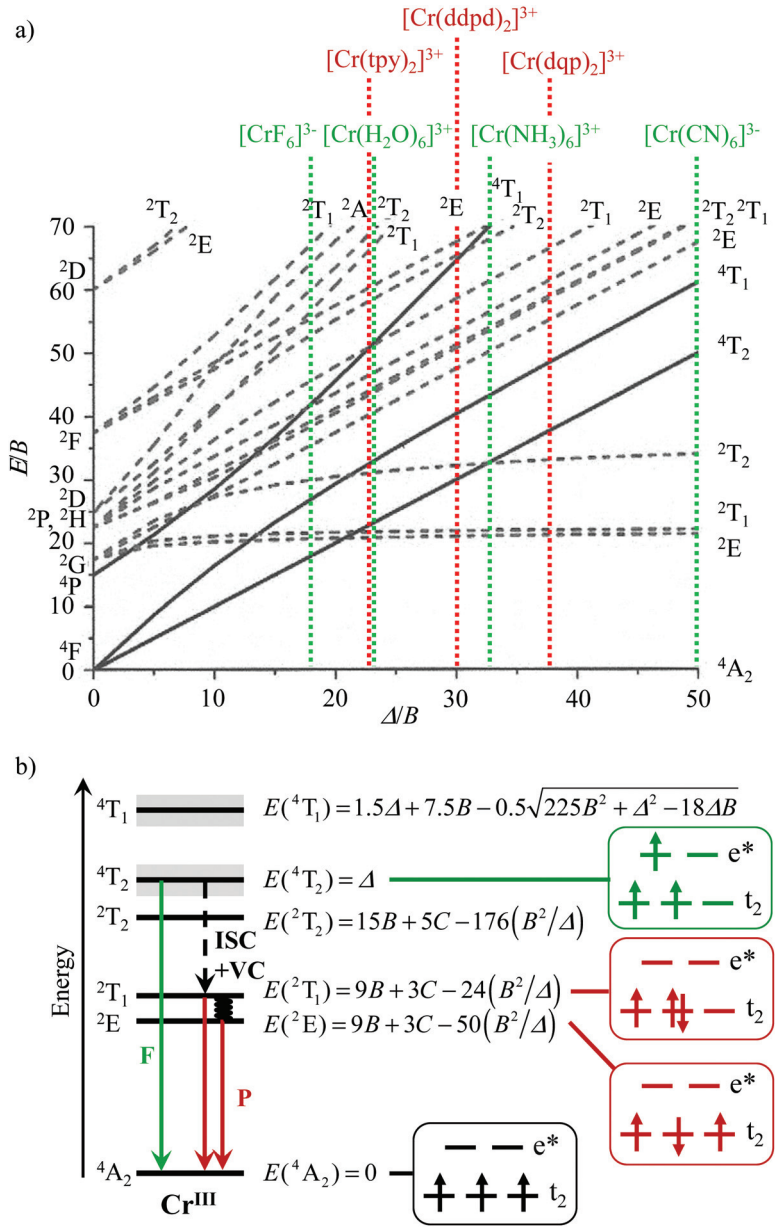


**Scheme 1** a) Tanabe–Sugano diagram (computed for $C/B$ = 4.5)[13] for the $d^3$ configuration in an octahedral ligand field highlighting some selected trivalent chromium complexes ($\Delta/B$ taken from Table S1,† tpy, ddpd and dqp are shown in Fig. 2) and (b) Perrin–Jablonski diagram showing (i) the energy levels of $[Cr^{III}X_6]$ chromophores with strong ligand-field, (ii) the microstates and (iii) the energies associated with the low lying metal-centred levels computed in terms of ligand field $\Delta$ and Racah parameters $B$ and $C$.[10] F = fluorescence, P = phosphorescence, ISC = intersystem crossing.

heterometallic assemblies,[20,21] which can be exploited for linear light-downshifting[32–34] or for light-upconversion.[35–39] Furthermore, energy (or electron) transfer can be also applied in bimolecular reactions, *e.g.* singlet oxygen formation or photoredox catalysis.[40–42]

For using these strong-field pseudo-octahedral $Cr^{III}$ coordination complexes as sensitizers or activators in polymetallic (supra)molecular assemblies, the parameters of the intermetallic energy transfer processes (EnT), which rely on through-space (Förster) and/or through-bond (Dexter) mechanisms, should be optimized.[43] Förster EnT is based on coulombic interactions operating between the multipole changes involved during the simultaneous relaxation process of the donor and the excitation of the acceptor.[43,44] Its efficiency decreases as $d^{-n}$, where $d$ is the distance between the donor and the acceptor and $n$ = 6, 8, 10 reflects the order of the multipole involved in the interaction. Its efficiency depends on the spectral overlap between the emission spectrum of the donor and the absorption spectrum of the acceptor. A spin rule is therefore implicit in this: for benefiting from an intense absorption spectrum, the associated transitions at each site must be spin-allowed. In contrast, Dexter EnT corresponds to a double elec-

 

tron-exchange which requires a strong electronic coupling, often obtained *via* chemical bonding between the donor and the acceptor. It involves the exchange integrals that account for the indistinguishability of the electrons in many-electron wavefunctions,[45] and it is therefore facilitated by good orbital overlap and short distance (decreases as $e^{-d}$). It does not collapse for local spin selection rules according that the spin of the whole assembly must be preserved.[43,46–48] Consequently, Dexter EnT is sometimes called 'triplet–triplet' EnT.[49] With this in mind, the building of short and directional molecular connectors between strong-field $Cr^{III}$ and its optical partners is highly wished. Simple two-atoms cyanide anions, previously used for the programming of magnetic exchange coupling in related systems,[3,4,14] appears to be a logical choice since the considerable covalence of the Cr–CN bonds is known to give strong-field and kinetically inert $[CrC_6]$ chromophores in $[Cr(CN)_6]^{3-}$, while the peripheral nitrogen atoms are able to interact with solvated trivalent lanthanide centers to give very efficient $Cr^{III} \rightarrow Nd^{III}$ and $Cr^{III} \rightarrow Yb^{III}$ energy transfers ($k_{EnT} \geq 10^8$ $s^{-1}$, Fig. 1).[33]

Whereas $[CrL_x(CN)_{(6-2x)}]^{(3-2x)-}$ (**L** = neutral didentate ligand, for example, 1,10-phenanthorline (phen) or 2,2′ bipyridine (bipy)) or $[CrL(CN)_3]$ (**L** = neutral facial tridentate ligand, for example, 1,4,7-triazacyclononane (tacn)) building blocks have been developed extensively for the design of magnetic clusters and assemblies,[2–4,14,19] their use as potential optical partners remained confidential. We are aware of one contribution exploring the systematic low-energy shift of the $Cr(^2T_1, ^2E \rightarrow {}^4A_2)$ phosphorescence emission spectra upon replacement of water with cyanide ligands around $Cr^{III}$ in $[Cr(H_2O)_n(CN)_{(6-n)}]^{(n-3)+}$ ($n$ = 1–6)[50] and a second report dealing with the emission spectra of *cis*-$[Cr(phen)(CN)_4]^-$, *cis*-$[Cr(bpy)_2(CN)_2]^+$ and *fac*-$[Cr(tren)(CN)_3]$.[51] On the other side, the recent need for replacing the costly and rarest 4d (Ru) and 5d (Re, Os, Ir) metals with earth abundant 3d (Cr),[27,28,35,52,54] Mn(I)[52,54] or 4d (Mo)[55] analogues boosted the use of the rigid tridentate polyaromatic ligands 2,2′:6′,2″-terpyridine (tpy), *N*,*N*′-dimethyl-*N*,*N*′-di(pyridine-2-yl)pyridine-2,6-diamine (ddpd) or 2,6-di(quinolin-8-yl)pyridine (dqp) ligands for tuning ligand-field and Racah parameters *via* chelate ring sizes, donor atoms and sterical constraints around $Cr^{III}$ in pseudo-octahedral homoleptic $[CrL_2]^{3+}$ (**L** = tpy, ddpd or dqp; Scheme 1a)[56–58] and heteroleptic $[Cr(L)(L')]^{3+}$ complexes.[59–63] Some preliminary efforts have been described for exploiting these strong-field $[CrN_6]$ chromophores as complex-as-ligands for connecting d and/or f-block partners,[64,65] but, to the best of our knowledge, the design of heteroleptic $[Cr(L)(CN)_3]$ building blocks is currently unknown despite the attractive perspectives of using short cyanide bridges for intermetallic connections while tuning the electronic properties of $Cr^{III}$ with the tridentate ligands. In this contribution we report on the explorative synthesis, characterization and photophysical properties of *mer*-$[Cr(L)(CN)_3]$ (**L** = tpy, ddpd and dqp, Fig. 2–4).

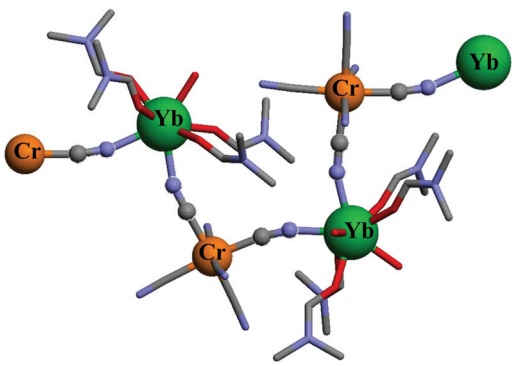


**Fig. 1** Structure of part of the one-dimensional chain of $\{[Cr(CN)_6][Yb(dmf)_4(H_2O)_2]\cdot H_2O\}_\infty$ highlighting the Cr–CN–Yb bridges.[33] Color code: C = grey, N = blue, O = red, Cr = orange, Yb = green.

## Results and discussion

### Synthesis and characterization of the heteroleptic *mer*-$[Cr(L)(CN)_3]$ (L = tpy, ddpd and dqp) complexes

Modern strategies used for the preparation of heteroleptic $Cr^{III}$ complexes are indebted to Kane-Maguire and co-workers, who took advantage of the unusual lability of the $Cr^{III}$–O(triflate) bond in $Cr(CF_3SO_3)_n$ adducts for the controlled synthesis of tri-didentate complexes.[66,67] Its extension for connecting two different tridentate binding units around six-coordinate $Cr^{III}$ was first reported by Constable and co-workers[59–61] and required the preparation of the *mer*-$[Cr(L)X_3]$ (X = Cl, Br) intermediates prior to react them with $HCF_3SO_3$ to form labile *mer*-$[Cr(L)(CF_3SO_3)_3]$ and HX. Although this method was proved to be effective with five-membered tpy-type chelating ligands,[59–61] its application with more basic six-membered ddpd and dqp ligands resulted in partial decomplexation and isolation of the protonated $[Hddpd]^+$ and $[Hdqp]^+$ ligands.[62,63] An alternative strategy relies on the weak solubility of the silver salts AgX in acetonitrile ($K_{sp}(AgCl) = 10^{-12.4}$, $K_{sp}(AgBr) = 10^{-13.2}$)[68] that can be easily separated from the soluble triflate $[Cr(L)(CF_3SO_3)_3]$ complex when $[Cr(ddpd)X_3]$ or $[Cr(dqp)X_3]$ are reacted with $AgCF_3SO_3$ in acetonitrile. Original attempts with $[Cr(ddpd)Cl_3]$ led to incomplete anion exchange, but starting from $[Cr(ddpd)Br_3]$ provided quantitative amount of $[Cr(ddpd)(CF_3SO_3)_3]$ and AgBr.[62] With this in mind, the preparation of the heteroleptic *mer*-$[Cr(L)Br_3]$ (**L** = tpy, ddpd and dqp) precursors was conducted with $CrBr_3\cdot 6H_2O$ as the metallic source and tpy (commercially available), ddpd[69] and dqp[70] as the tridentate ligands (Fig. 2). The characterization of the poorly soluble *mer*-$[Cr(L)Br_3]$ complexes (only slightly soluble in DMF or in acetonitrile) is challenging because (i) high resolution NMR spectroscopy is hampered by the long electronic relaxation time of the $Cr(^4A_2)$ paramagnetic ground state and (ii) the lack of permanent charge limits mass spectrometry to the detection of dissociated $[Cr(L)Br_n]^{(3-n)+}$ ($n$ = 1, 2) derivatives.

The IR spectra (Fig. 4 and Fig. S1†) combined with satisfying elemental analyses (Table S2†) confirmed the presence of both ligand **L** and $CrBr_3$ in the isolated microcrystalline powders. Slow diffusion of diethyl ether into DMF solutions

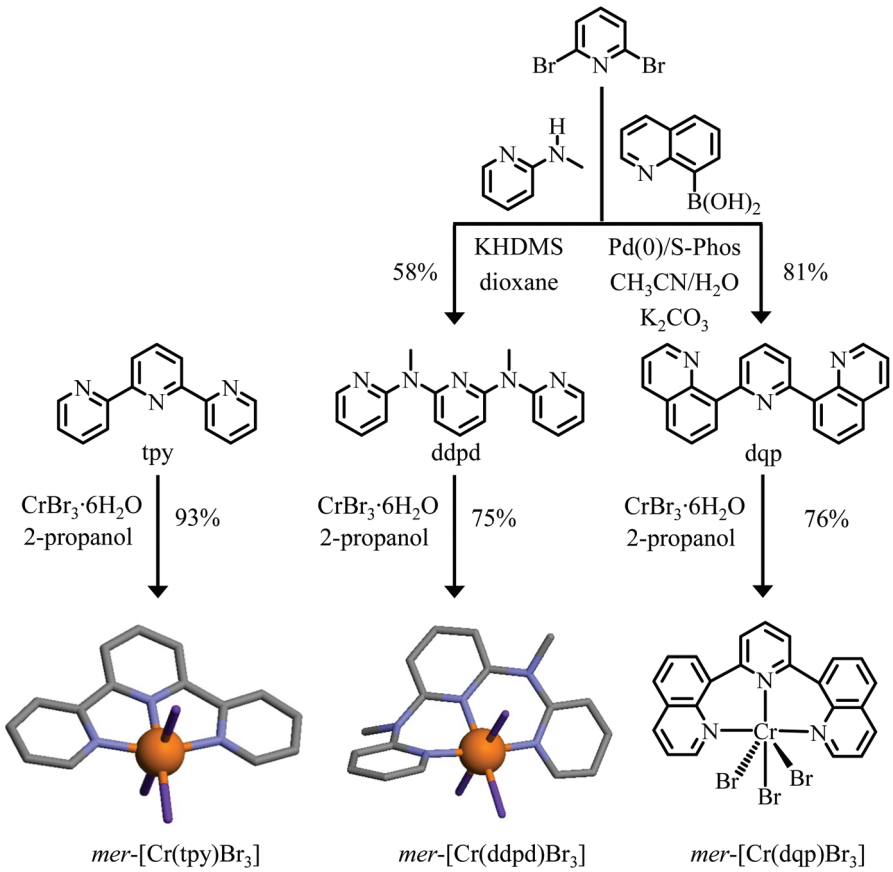


**Fig. 2** Syntheses and structures of *mer*-[Cr(tpy)$Br_3$], *mer*-[Cr(ddpd)$Br_3$][62] and *mer*-[Cr(dqp)$Br_3$]. Color code: C = grey, N = blue, Br = purple, Cr = orange. H atoms have been omitted for clarity.

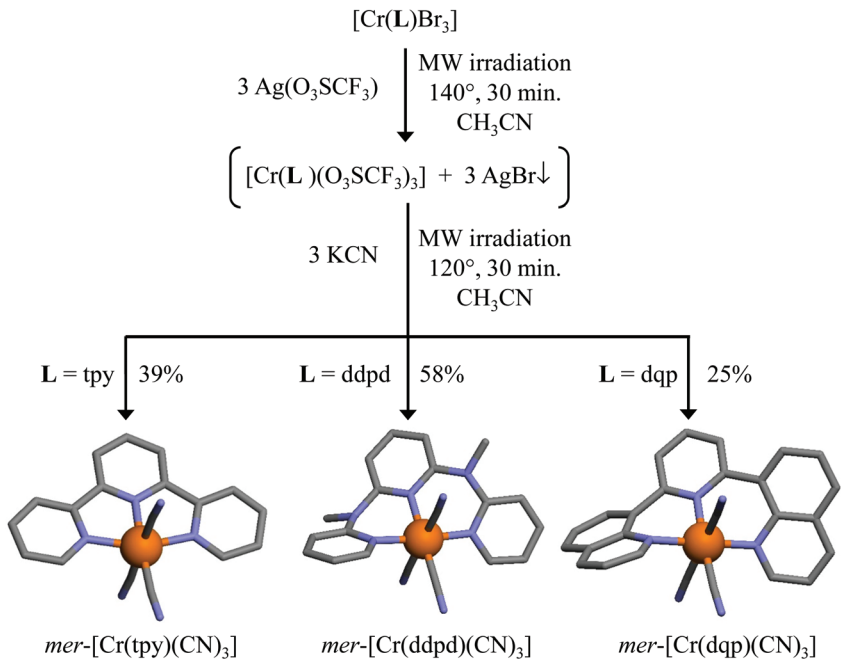


**Fig. 3** Syntheses and structures of *mer*-[Cr(L)$(CN)_3$] (L = tpy, ddpd, dqp). Color code: C = grey, N = blue, Cr = orange. H atoms have been omitted for clarity.

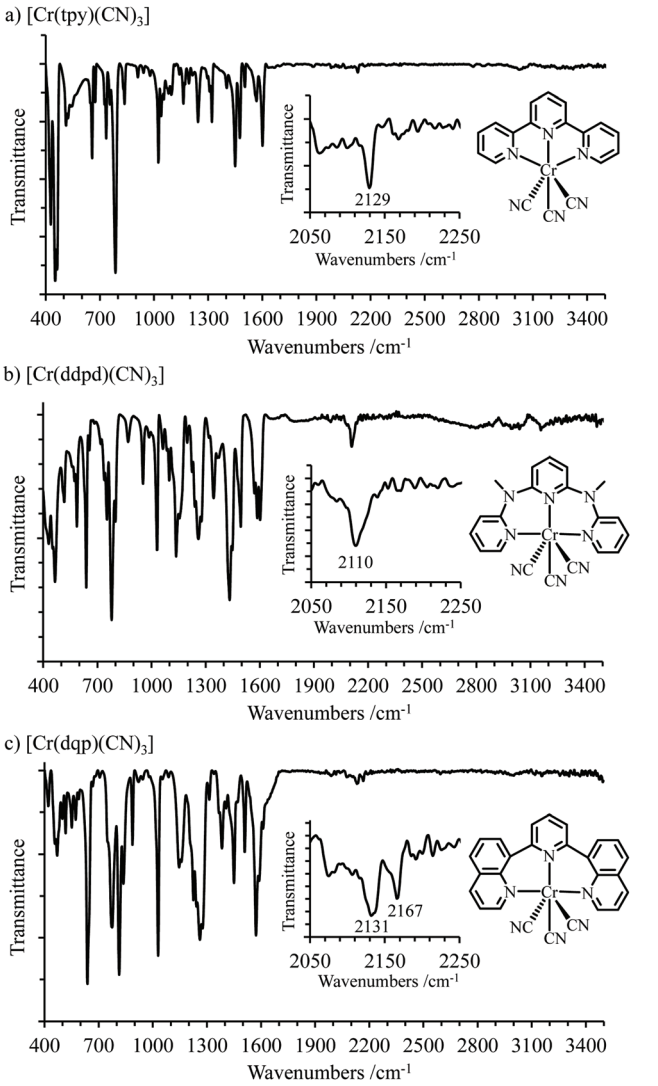


Fig. 4 IR spectra of *mer*-[Cr(L)(CN)$_3$] (L = tpy, ddpd, dqp) recorded in the solid state at 293 K.

provided single crystal suitable for X-ray diffraction studies for [Cr(tpy)Br$_3$] (Fig. S2† and Tables S3–S5†) and [Cr(ddpd)Br$_3$],[62] but we were unable to crystallize [Cr(dqp)Br$_3$] (Fig. 2). In line with the molecular structures reported previously for [Cr(**L**)Cl$_3$] (**L** = tpy,[71] ddpd[64] and dqp,[63] Table 1 entries 1–3), the tridentate ligands are all meridionally bound to Cr$^{III}$ (Fig. 2), but only the fused five-membered chelate rings in [Cr(tpy)Br$_3$] are compatible with a rough planar arrangement of the aromatic units (3.6° ≤ interplanar angles ≤ 7.2°, Fig. 2 and Table S5†), whereas the six-membered chelate rings in [Cr(ddpd)Br$_3$] produce an helical twist of the polyaromatic ligand (46.8° ≤ interplanar angles ≤ 46.9°, Fig. 2).[62]

Since the three halogen atoms occupy the three missing vertices of the pseudo-octahedron around Cr$^{III}$ with mainly no constraint, [Cr(tpy)X$_3$] (X = Cl, Br) are close to fit the criteria of the non-chiral $C_{2v}$ point group whereas [Cr(ddpd)X$_3$] and [Cr(dqp)Cl$_3$] belong to the chiral $C_2$ point group and crystallize as racemic mixtures. The amount of deviation from a perfect octahedral arrangement of the six donor atoms around the central metal can be obtained by computing $\Sigma = \sum_{i=1}^{12} |90 - \phi_i|$, where $\phi_i$ are the 12 cisoid bond angles around the Cr$^{3+}$ cation (Table 1, column 8). The latter parameter is twice larger for [Cr(tpy)X$_3$] (46.7 ≤ $\Sigma$ ≤ 59.9°) than for [Cr(ddpd)X$_3$] (21.6 ≤ $\Sigma$ ≤ 22.3°) and [Cr(dqp)Cl$_3$] ($\Sigma$ = 30°), a distortion highlighted by the *trans*-N–Cr–N bite angles which reach 156–157° for [Cr(tpy)X$_3$], but are close to be linear for [Cr(ddpd)X$_3$] and [Cr(dqp)Cl$_3$] (172–173°). As expected, the replacement of X = Cl with X = Br in [Cr(**L**)X$_3$] (**L** = tpy and ddpd) produces only very minor changes except for a rough 6% increase of the Cr–X bond lengths (Table 1, column 4 and Fig. S3†).

Treatment of *mer*-[Cr(**L**)Br$_3$] with AgCF$_3$SO$_3$ was carried out in acetonitrile under microwave irradiation. The resulting precipitates of AgBr were removed by filtration, while peaks observed at *m*/*z* = 583 ([Cr(tpy)(CF$_3$SO$_3$)$_2$]$^+$), *m*/*z* = 641 ([Cr(ddpd)(CF$_3$SO$_3$)$_2$]$^+$) and *m*/*z* = 683 ([Cr(dqp)(CF$_3$SO$_3$)$_2$]$^+$) in the ESI-MS spectra confirmed the formation of the soluble [Cr(**L**)(CF$_3$SO$_3$)$_3$] complexes in the filtrates. The latter complexes were not isolated, and subsequent reactions with KCN under microwave heating provided the final complexes [Cr(**L**)(CN)$_3$] (**L** = tpy, ddpd, dqp, Table S2†) in low to moderate yields (Fig. 3). These complexes are reasonably soluble in polar solvents (DMF, water, acetonitrile, methanol), but insoluble in less polar organic solvents. Single crystals suitable for X ray diffraction (XRD) were obtained after recrystallization in hot water for [Cr(tpy)(CN)$_3$] (Fig. S4, and Tables S6–S8†) and after slow evaporation of solutions containing complexes in acetone/water (1 : 1) or methanol/water (5 : 1) for [Cr(ddpd)(CN)$_3$]·2H$_2$O (Fig. S5, and Tables S9–S11†) and [Cr(dqp)(CN)$_3$]·3.28H$_2$O (Fig. S6, and Tables S12–S14†), respectively. The molecular structures of *mer*-[Cr(**L**)(CN)$_3$] (**L** = tpy, ddpd, dqp, Fig. 3) are very similar to those previously discussed for related *mer*-[Cr(**L**)X$_3$] complexes (X = Cl, Br, Fig. S7†), except for the observation of shorter Cr–C bonds (2.07 to 2.09 Å) compared with Cr–X bonds which cover the 2.32–2.49 Å range, but similar to 2.08(2) Å reported for Cr–C bonds in K$_3$[Cr(CN)$_6$] (Table 1). A thorough analysis of the packing of the crystal structures of [Cr(tpy)(CN)$_3$], [Cr(ddpd)(CN)$_3$]·2H$_2$O and [Cr(dqp)(CN)$_3$]·3.28H$_2$O show only weak CN···HO interactions when water molecules are present in the crystal structure together with some weak interligand π-stacking involving layers of complexes (Fig. S8–S11†). No trace of strong intermolecular bridges involving cyanide anions could be detected so that *mer*-[Cr(**L**)(CN)$_3$] exist as well-defined molecular entities in the solid state. The IR spectra display very weak CN stretching bands in the 2100–2170 cm$^{-1}$ domain where three IR-active bands are expected for [Cr(tpy)(CN)$_3$] ($C_{2v}$ symmetry: 2A$_1$ + B$_1$, Fig. 4a) and for [Cr(ddpd)(CN)$_3$] or [Cr(dqp)(CN)$_3$] ($C_2$ symmetry: 2A + B, Fig. 4b and c).[74] These stretching vibrations are located at higher energy than those found for non-complexed cyanide anion in KCN (2080 cm$^{-1}$)[75] because the poor π-accepting CN$^-$ ligands maximize their σ-donation upon complexation to a d-block cation. This tends to raise the $\nu$(CN) stretching frequencies since electrons are removed from

Table 1 Average bond lengths, bite angles and total distortion from octahedral geometry $\Sigma$[a] observed in the crystal structures of the heteroleptic *mer*-[Cr(L)$X_3$] (L = tpy, ddpd and dqp, X = Cl, Br, CN) complexes and of their homoleptic parent [Cr$L_2$]$X_3$ and $K_3$[Cr(CN)$_6$] complexes[b]

| Complex | Cr–$N_{central}$ / Å | Cr–$N_{distal}$/ Å | Cr–X/Å | Bite angle /° *trans*-N–Cr–N | Bite angle /° *trans*-N–Cr–X | Bite angle /° *trans*-X–Cr–X | $\Sigma$/° | Ref. |
|---|---|---|---|---|---|---|---|---|
| [Cr(tpy)$Cl_3$] | 1.992 | 2.075(5) | 2.32(2) | 157.02 | 178.48 | 174.57 | 59.9 | 71 |
| [Cr(ddpd)$Cl_3$] | 2.071 | 2.068(5) | 2.33(1) | 172.82 | 178.17 | 179.11 | 21.6 | 64 |
| [Cr(dqp)$Cl_3$] | 2.059 | 2.077(0) | 2.34(2) | 173.81 | 180 | 178.21 | 30.0 | 63 |
| [Cr(tpy)$Br_3$] | 1.989 | 2.074(2) | 2.47(2) | 156.71 | 176.02 | 176.30 | 46.7 | This work |
| [Cr(ddpd)$Br_3$] | 2.074 | 2.07(1) | 2.49(1) | 173.06 | 177.17 | 178.62 | 22.3 | 62 |
| [Cr(tpy)$(CN)_3$] | 1.993 | 2.07(4) | 2.07(1) | 156.84 | 175.17 | 176.93 | 65.4 | This work |
| [Cr(ddpd)$(CN)_3$] | 2.041 | 2.087(0) | 2.085(4) | 174.59 | 180 | 178.90 | 19.8 | This work |
| [Cr(dqp)$(CN)_3$] | 2.044 | 2.072(1) | 2.076(8) | 176.71 | 175.94 | 173.59 | 25.6 | This work |
| [Cr(tpy)$_2$]$(PF_6)_3$ | 1.986(1) | 2.054(9) | — | 157.12(8) | — | — | 102.0 | 59 |
| [Cr(ddpd)$_2$]$(BF_4)_3$ | 2.042(4) | 2.046(5) | — | 170.87(2) | — | — | 36.0 | 56 |
| [Cr(dqp)$_2$]$(CF_3SO_3)_3$ | 2.049(4) | 2.063(3) | — | 174.8(3) | — | — | 28.9 | 58 |
| [Cr(dqc)$_2$]$PF_6$ [c] | 1.962(4) | 2.109(3) | — | 173.69(8) | — | — | 39.0 | 72 |
| $K_3$[Cr(CN)$_6$] | — | — | 2.08(2) | — | — | 179.0(6) | 6.6 | 73 |

[a] *Æ©* is calculated with the formula $\Sigma = \sum_{i=1}^{12} |90 - \phi_i|$ where $\phi_i$ are the 12 cisoid bond angles around the $Cr^{III}$ metal. [b] The values given between parentheses correspond to the standard deviation when several distances or bond angles are considered. [c] dpc$^-$ is the tridentate 3,6-di-*tert*-butyl-1,8-di(pyridine-2-yl)-carbazolate ligand.

the slightly anti-bonding cyanide-based σ orbital, a process which reinforces the $CN^-$ force constant.[75] Following the thorough analysis of Jones,[76] one expects that the changes in dipole moment accompanying the characteristic oscillations of cyanides bound to electron-poor $Cr^{III}$ are weak, but the faint absorptions recorded for *mer*-[Cr(**L**)$(CN)_3$] merit to be stressed here (Fig. 4) and compared with the much stronger peaks observed for $K_3$[Cr(CN)$_6$].[76]

## Photophysical properties of the heteroleptic *mer*-[Cr(L)$(CN)_3$] (L = tpy, ddpd and dqp) complexes

Based on their molecular structures observed in the solid state, *mer*-[Cr(tpy)$(CN)_3$] can be assigned to the $C_{2v}$ point group and *mer*-[Cr(ddpd)$(CN)_3$] and *mer*-[Cr(dqp)$(CN)_3$] to $C_2$ point group, both possessing only mono-dimensional irreducible representations. Consequently, the three standard d–d transitions, *i.e.* the two spin-forbidden Cr($^2$E ↔ $^4$A$_2$), Cr($^2$T$_1$ ↔ $^4$A$_2$) and the spin-allowed Cr($^4$T$_2$ ↔ $^4$A$_2$) transitions, which are detected as unsplit bands in the absorption and/or emission spectra of strong-field octahedral $Cr^{III}$ complexes ($O_h$ symmetry, Scheme 1a), are expected to be split in *mer*-[Cr(**L**)$(CN)_3$] because the excited E and T levels transform into $A_1$, $A_2$, $B_1$ and $B_2$ ($C_{2v}$) or A and B ($C_2$) representations. However, as observed for the [Cr$N_6$] chromophores found in the homoleptic $D_{2(d)}$ symmetrical [Cr(**L**)$_2$]$^{3+}$ (**L** = tpy, ddpd and dqp) analogues,[56–58,64] the deviation from local $O_h$ symmetry is small for the [Cr$C_3N_3$] chromophores found in *mer*-[Cr(**L**)$(CN)_3$] (Fig. 3 and Table 1). The detection of only minor additional splitting in the absorption and emission spectra (Fig. 5–7 and S21–S23†) justifies the use of (i) a simplified mathematical treatment of the optical spectra pertinent to $O_h$ symmetry (Scheme 1b) and (ii) original labels reminiscent of $O_h$ symmetry for these complexes.[6,8–10,64,77] With this in mind, the ligand field and Racah parameters are obtained from the experimental energies of the excited levels by solving eqn (1)–(3) (Table 2, entries 8–10).[58,64]

$$E(^4T_2) = \Delta \quad (1)$$

$$E(^2T_1) - E(^2E) = 26(B^2/\Delta) \quad (2)$$

$$E(^2T_1) = 9B + 3C - 24(B^2/\Delta) \quad (3)$$

The situation is more tricky for the heteroleptic *mer*-[Cr(**L**)$X_3$] (X = Cl, Br) complexes because the [Cr$N_3X_3$] coordination spheres deviate significantly from octahedral symmetry and we prefer to not derive oversimplified ligand parameters for these low-symmetrical complexes (Table 2).

The absorption spectra are dominated by intense ligand-centered π* ← π transitions together with LMCT and MC transitions covering the UV-visible domain (Fig. 5); an assignment confirmed by theoretical TD-DFT calculations (Tables S15–S20 and Fig. S12–S20†). At lower energies, the TD-DFT calculations predict three sets of spin-allowed metal-centered d–d transitions located at 22 170–22 620 cm$^{-1}$, 25 445–28 190 cm$^{-1}$ and 31 350–32 570 cm$^{-1}$ for [Cr(tpy)$(CN)_3$] (Fig. S13†), which are reminiscent of the three Cr($^4$T$_{1,2}$ ← $^4$A$_2$) transitions expected in octahedral symmetry (Scheme 1a). Comparison with the experimental absorption spectrum (Fig. S13b†) allows to assign the weak band at 22 370 cm$^{-1}$ to Cr($^4$T$_2$ ← $^4$A$_2$), which gives a direct estimation of $\Delta$ (eqn (1), Table 2 column 8). The same procedure can be applied for [Cr(ddpd)$(CN)_3$] (Fig. S16 and S17†) and [Cr(dqp)$(CN)_3$] (Fig. S19 and S20†) to give slightly larger ligand-field parameters $\Delta$ = 24 000–24 500 cm$^{-1}$ (Table 2, column 8); a result in line with the replacement of five-membered chelate rings in tpy with six-membered rings in ddpd and dqp.[56–58] The forbidden Cr($^2$T$_1$,$^2$E ← $^4$A$_2$) spin–flip transitions cannot be detected in solution at the largest accessible concentrations (10–50 mM due to limited solubility), which implies $\varepsilon$ < 0.1 M$^{-1}$ cm$^{-1}$.

 

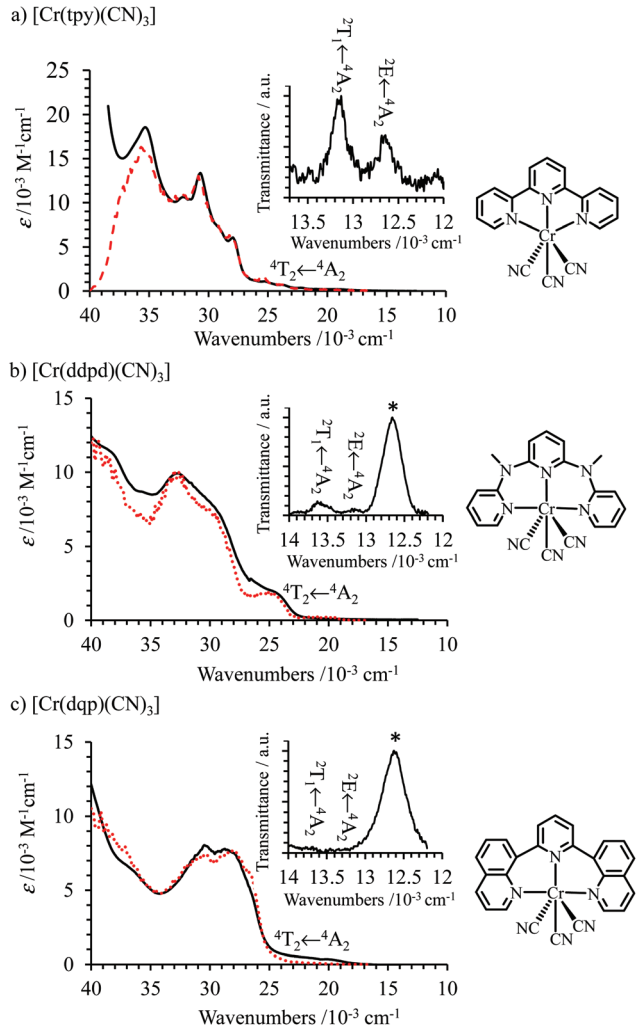


Fig. 5 Absorption (black full traces) and normalized excitation (red dotted traces, analysis fixed on the $Cr(^2E \rightarrow {}^4A_2)$ spin–flip emission band) spectra recorded for (a) $[Cr(tpy)(CN)_3]$ ($c$ = 1.40 × $10^{-5}$ M in DMF at 293 K, for excitation $\tilde{\nu}_{analysis}$ = 12 706 $cm^{-1}$), (b) $[Cr(ddpd)(CN)_3]$ ($c$ = 1.75 × $10^{-5}$ M in $CH_3CN$ at 293 K, for excitation $\tilde{\nu}_{analysis}$ = 13 175 $cm^{-1}$) and (c) $[Cr(dqp)(CN)_3]$ ($c$ = 1.75 × $10^{-5}$ M in $CH_3CN$ at 293 K, for excitation $\tilde{\nu}_{analysis}$ = 13 228 $cm^{-1}$). The NIR inset spectra correspond to transmittance absorption spectra recorded for solid state single crystals at 293 K. * represents the hypothetical OH overtone.

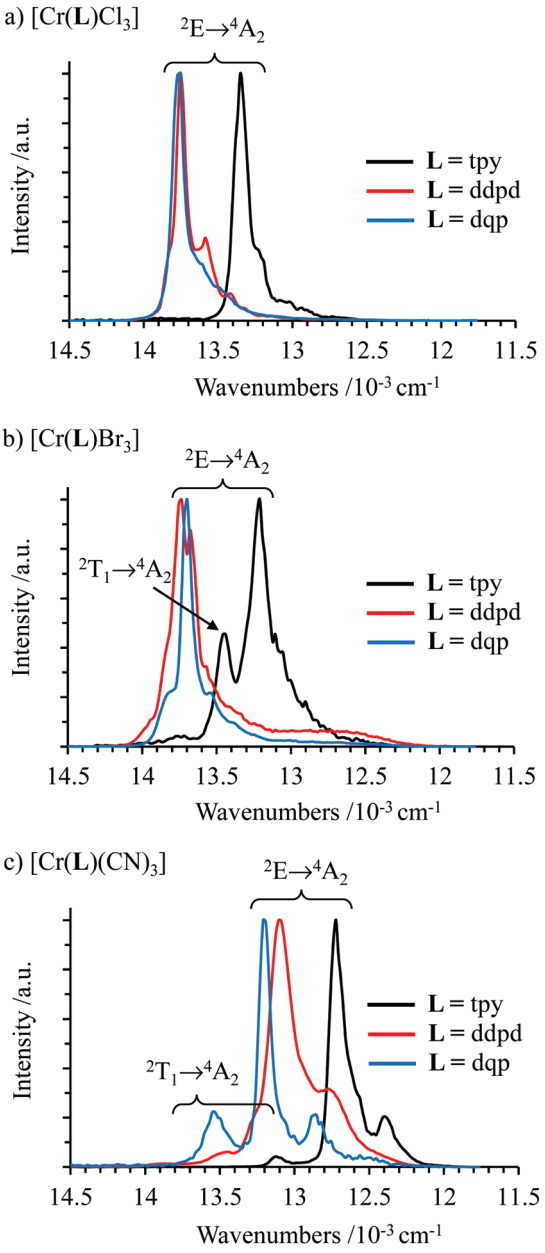


Fig. 6 (a)–(c) Emission spectra ($\tilde{\nu}_{excitation}$ = 28 750 $cm^{-1}$) recorded for $[Cr(L)X_3]$ (L = tpy, ddpd, dqp; X = Cl, Br, CN) in frozen solution at 77 K ($c$ = 2 × $10^{-5}$ M; $[Cr(L)Cl_3]$, $[Cr(L)Br_3]$ and $[Cr(tpy)(CN)_3]$ in DMF; $[Cr(ddpd)(CN)_3]$ and $[Cr(dqp)(CN)_3]$ in $CH_3CN$ : $C_2H_5CN$ 3 : 1).

Excitations at $\lambda_{exc}$ = 350 nm ($\tilde{\nu}_{ex}$ = 28 570 $cm^{-1}$) of all heteroleptic $[Cr(L)X_3]$ (L = tpy, ddpd, dqp; X = Cl, Br, CN) complexes in frozen solution at 77 K induce red to near-infrared emissions, which can be assigned to the spin–flip $Cr(^2T_1, {}^2E \rightarrow {}^4A_2)$ transitions, the energies of which follow the trends $[Cr(L)Cl_3] \approx [Cr(L)Br_3] > [Cr(L)(CN)_3]$ for a given tridentate ligand L and $[Cr(dqp)X_3] \geq [Cr(ddpd)X_3] \gg [Cr(tpy)X_3]$ for a given anion $X^-$ (Fig. 6).

While the phosphorescence of the halogenido complexes $[Cr(L)Cl_3]$ and $[Cr(L)Br_3]$ is too weak to be detected at room temperature with our setup, detectable emissions can be observed in these conditions for $[Cr(L)(CN)_3]$ (Fig. 7). The larger intensities observed for the high-energy $Cr(^2T_1 \rightarrow {}^4A_2)$ bands at room temperature results from the thermally-induced population of the $Cr(^2T_1)$ excited levels by the close $Cr(^2E)$ states.[56,57,78] The overall quantum yields recorded in de-aerated solutions at 293 K upon 22 990 $cm^{-1}$ excitation ($\lambda_{exc}$ = 435 nm) are 0.2% for $[Cr(ddpd)(CN)_3]$, 0.08% for $[Cr(dqp)(CN)_3]$ and 0.0001% for $[Cr(tpy)(CN)_3]$.

The associated room-temperature excitation spectra recorded upon monitoring the $Cr(^2E \rightarrow {}^4A_2)$ phosphorescence in $[Cr(L)(CN)_3]$ match the absorption spectra (Fig. 5) and demonstrate that the Cr-centered emission can be sensitized

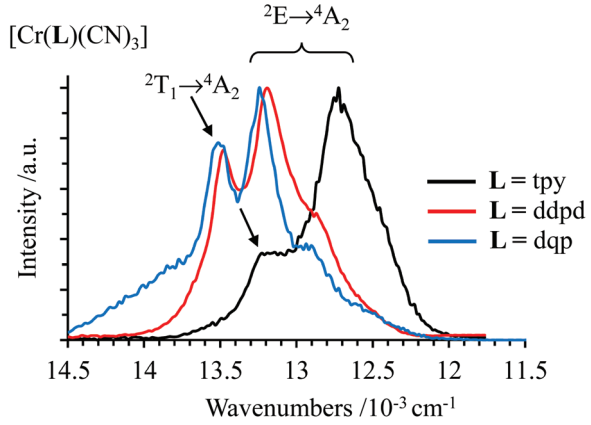


**Fig. 7** Emission spectra ($\tilde{\nu}_{excitation} = 28\,750\ cm^{-1}$) recorded for [Cr(L)$(CN)_3$] (L = tpy, ddpd, dqp) solution at 293 K ($c = 2 \times 10^{-5}$ M; [Cr(tpy)$(CN)_3$] in DMF, [Cr(ddpd)$(CN)_3$] and [Cr(dqp)$(CN)_3$] in $CH_3CN$).

by both LMCT, metal-centered and ligand-centered $\pi^* \leftarrow \pi$ transitions. In order to better characterize the spin–flip $Cr(^2T_1,^2E \leftrightarrow {}^4A_2)$ transitions, the transmittance spectra of solid state samples of pure [Cr(**L**)$X_3$] (**L** = tpy, ddpd, dqp; X = Cl, Br, CN) were recorded in the NIR region (shown as insets in Fig. 5) and compared with the corresponding emission spectra in Fig. S21–S23.† Firstly, it is worth stressing here that the intensities of the spin-forbidden $Cr(^2T_1,^2E \leftarrow {}^4A_2)$ transitions are so weak that they correspond to only minor distortions from the baselines of the solid-state transmittance spectra and require thorough mathematical corrections to separate true spectroscopic signals from the background. This being said, we nevertheless observe that the intensities of the $Cr(^2T_1,^2E \leftarrow {}^4A_2)$ absorption bands in solid state samples depend on the nature of the anions bound to $Cr^{III}$ and decrease with their electronegativities $X = Cl^- > Br^- > CN^-$. As expected for these low-symmetry $C_2$ or $C_{2v}$ complexes, the splitting of the $^2E$ and $^2T_1$ excited levels produce more than the two spin–flip transitions reminiscent of $O_h$ point group (see for instance *mer*-[Cr(dqp)$Cl_3$] in Fig. S23†), but the comparison of emission/absorption spectra allows to state that (i) the minor Stokes shifts rarely exceed 50 $cm^{-1}$, (ii) room temperature emission spectra magnify the emission of the $Cr(^2T_1)$ level located at higher energy (thermal equilibrium) and (iii) the pseudo-octahedral description of the spin–flip transitions as arising from $Cr(^2T_1,^2E \leftrightarrow {}^4A_2)$ is satisfying for the [$CrC_3N_3$] chromophores found in [Cr(**L**)$(CN)_3$]. Having the estimations of the energies of the $Cr(^2E)$ and $Cr(^2T_1)$ levels in hand (Table 2, column 3 and 4), eqn (2) and (3) provide the nephelauxetic parameters collected in Table 2 (columns 9 and 10). The stepwise replacement of the two tridentate chelate $N_3$ units found in $[CrL_2]^{3+}$ with monodentate $CN^-$ ligands to give *mer*-[Cr**L**$(CN)_3$] and $[Cr(CN)_6]^{3-}$ is accompanied by an average 150 $cm^{-1}$ decrease of the Racah *B* parameter (*i.e.* an increase of the nephelauxetic effect and charge delocalization) for the coordination of the three first cyanide anions and a further, but smaller, reduction of *B* for the substitution of the remaining tridentate ligand to eventually reach $B = 480\ cm^{-1}$ for $[Cr(CN)_6]^{3-}$ (ref. 79) This trend is obviously more pronounced for the successive replacement of the constrained five-membered chelate rings found in $[Cr(tpy)_2]^{3+}$ than of the looser six-membered rings in $[Cr(ddpd)_2]^{3+}$ and $[Cr(dqp)_2]^{3+}$.

Surprisingly, the solid-state transmittance spectra recorded for single crystals of [Cr(ddpd)$(CN)_3$] (Fig. 5b) and of [Cr(dqp)$(CN)_3$] (Fig. 5c) display an additional weak absorption band centered at 12 600 $cm^{-1}$ (794 nm, marked with an asterisk), the intensity of which is still one order of magnitude larger than that measured for the spin-forbidden $Cr(^2T_1,^2E \leftarrow {}^4A_2)$ transitions. These absorption bands are fully reproducible for the latter two complexes, but they are lacking for all the other studied heteroleptic [Cr(**L**)$X_3$] complexes (**L** = tpy, X = Cl, Br, CN and **L** = ddpd, dqp, X = Cl, Br; Fig. S21–S23†) and for the free ligands. We must confess that we are not able to propose a

**Table 2** Energies and lifetimes ($\tilde{\nu}_{excitation} = 28\,750\ cm^{-1}$) of the emissive $Cr^{III}$-centered levels and estimated ligand-field *Δ* and Racah parameters *B* and *C* for the heteroleptic *mer*-[Cr(L)$X_3$] (X = Cl, Br, CN) and their homoleptic parent $[Cr(L)_2]^{3+}$ (L = tpy, ddpd and dqp) complexes

| Complex | Solvent | $E(^2T_1)$ / $cm^{-1}$ | $E(^2E)$ / $cm^{-1}$ | $\tau(^2E)$ / μs 77 K[b] | $\tau(^2E)$/ μs 293 K[a] | $\tau(^2E)$/ μs 293 K[b] | *Δ*/ $cm^{-1}$ | *B*/ $cm^{-1}$ | *C*/ $cm^{-1}$ | *Δ*/ *B* | Ref. |
|---|---|---|---|---|---|---|---|---|---|---|---|
| [Cr(tpy)$Cl_3$] | DMF | 13 602 | 13 175 | 690(10)[c] | — | — | 16 694 | 697 | 2786 | 24.0 | 64 |
| [Cr(ddpd)$Cl_3$] | DMF | 14 040 | 13 755 | 1580(15) | — | — | — | — | — | — | This work |
| [Cr(dqp)$Cl_3$] | DMF | 14 040 | 13 670 | 1560(15) | — | — | — | — | — | — | This work |
| [Cr(tpy)$Br_3$] | DMF | 13 460 | 13 210 | 110(5) | — | — | — | — | — | — | This work |
| [Cr(ddpd)$Br_3$] | DMF | — | 13 736 | 1560(15) | — | — | — | — | — | — | This work |
| [Cr(dqp)$Br_3$] | DMF | — | 13 698 | 1540(15) | — | — | — | — | — | — | This work |
| [Cr(tpy)$(CN)_3$] | DMF | 13 262 | 12 610 | 1020(20) | $3.12(1) \times 10^{-3}$ | $2.94(1) \times 10^{-3}$ | 22 370 | 670 | 2565 | 33.4 | This work |
| [Cr(ddpd)$(CN)_3$] | $CH_3CN$ | 13 605 | 13 089 | 3590(20) | 79(3) | 10.1(2) | 24 540 | 520 | 3030 | 47.2 | This work |
| [Cr(dqp)$(CN)_3$] | $CH_3CN$ | 13 513 | 13 192 | 4020(20) | 13.0(6) | 6.8(2) | 24 100 | 480 | 3140 | 50.2 | This work |
| $[Cr(tpy)_2](PF_6)_3$ | $CH_3CN$ | 12 953 | 13 584 | 670(10) | 0.14 | - | 18 750 | 790 | 2512 | 23.7 | 62 and 64 |
| $[Cr(ddpd)_2](BF_4)_3$ | $CH_3CN$ | 13 387 | 12 788 | 1300(15) | 975(10) | 51(5) | 22 990 | 659 | 2638 | 34.9 | 56 and 64 |
| $[Cr(dqp)_2](CF_3SO_3)_3$ | $H_2O$ | 13 949 | 12 903 | 3070(20) | 1270(10) | 83(5) | 24 937 | 656 | 2791 | 38.0 | 58 and 62 |
| $[Cr(dqc)_2]PF_6$ [d] | $CH_3CN$ | — | 9370 | 2.0 | — | — | 19 200 | 470 | 1880 | 40.9 | 53 and 72 |
| $K_3[Cr(CN)_6]$ | $H_2O$ | — | 12 400 | 4200 | — | — | 26 600 | 480 | 2800 | 55.4 | 50 and 79 |

[a] Deaerated solution. [b] Non-deaerated solution. [c] Recorded at 10 K. [d] $dpc^-$ is the tridentate 3,6-di-*tert*-butyl-1,8-di(pyridine-2-yl)-carbazolate ligand.

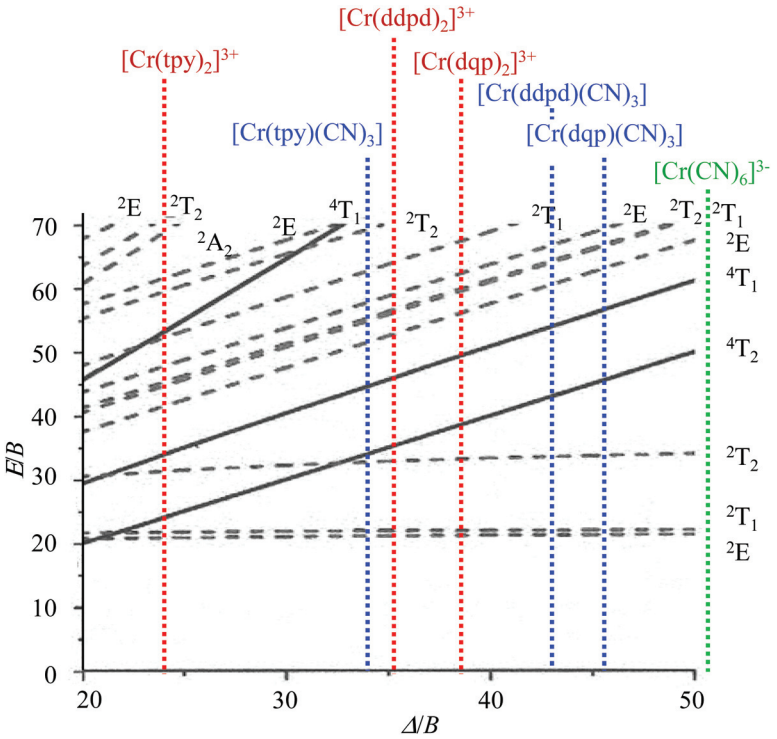


**Scheme 2** Tanabe–Sugano diagram for the $d^3$ configuration in an octahedral ligand field (computed for $C/B$ = 4.5) highlighting the pseudo-octahedral [$CrN_6$] (red), [$CrC_3N_3$] (blue) and [$CrC_6$] (green) chromophores. $\Delta/B$ taken from Table 2.

fully convincing explanation, but one notices that crystals of [Cr(ddpd)$(CN)_3$] (Table S9†) and [Cr(dqp)$(CN)_3$] (Table S12†) contain co-crystallized water molecules, the fourth harmonic of which is expected to give a weak broad absorption band centered at 13 300 $cm^{-1}$ in the pure liquid (750 nm, $\varepsilon \approx 2 \times 10^{-4}$ $M^{-1}$ $cm^{-1}$).[80,81] On the contrary, crystals of [Cr(tpy)$(CN)_3$] do not contain residual water molecules in the unit cell (Table S6†).

Finally, the $Cr(^2E)$ excited lifetimes of 1.0–4.0 ms observed for [Cr(**L**)$(CN)_3$] in frozen solution at 77 K (Table 2, column 5) are intermediate between 4.2 ms reported for $[Cr(CN)_6]^{3-}$ (an octahedral [$CrC_6$] chromophore, Table 2, entry 13)[50] and 0.67–3.0 ms characterizing $[Cr(\mathbf{L})_2]^{3+}$ ([$CrN_6$] chromophores Table 2, entries 10–12).[56,58,62,64] As usual, the longest lifetimes are found for **L** = dqp, which forms six-membered chelate rings in [Cr(dqp)$(CN)_3$] and $[Cr(dqp)_2]^{3+}$, displays minor distortions from octahedral symmetry for the six bound nitrogen donor atoms and possesses only two rotational degrees of freedom.[58] At room temperature in solution, the non-radiative deactivation pathways become particularly efficient in the heteroleptic [Cr(**L**)$(CN)_3$] complexes and the $Cr(^2E)$ excited lifetimes drop to a few microseconds for **L** = ddpd, dqp and a few nanoseconds for **L** = tpy (Table 2, columns 6 and 7).

## Conclusion

Although some rare cases of facial isomers have been reported for homoleptic $[M(ddpd)_2]^{z+}$ (M = $Co^{II}$ or $V^{III}$),[82] none has been described with M = $Cr^{III}$ with any of the tridentate polyaromatic ligands tpy, ddpd and dqp used in this work. In agreement with these observations the tridentate ligands in the studied heteroleptic [Cr(**L**)$X_3$] complexes (**L** = tpy, ddpd, dqp, X = Cl, Br, CN) are systematically meridionally tri-coordinated around $Cr^{III}$, thus leaving three meridional positions for the anionic co-ligands. As found for the parent homoleptic $[Cr(\mathbf{L})_2]^{3+}$ complexes, the deviation from octahedral symmetry of the six donor atoms in the first coordination sphere depends on the size of the chelate rings. It severely decreases in going from five-membered chelates produced by bound **L** = tpy, to six-membered chelates found with **L** = ddpd, dqp. The photophysical properties reflect these distortions with a smaller ligand-field strength for *mer*-[Cr(tpy)$(CN)_3$] compared with *mer*-[Cr(**L**)$(CN)_3$] (**L** = ddpd, dqp). Additionally, the binding of cyanide anions to $Cr^{III}$ reinforces the nephelauxetic effect and shift the $\Delta/B$ values of *mer*-[Cr(**L**)$(CN)_3$] toward the right of the Tanabe–Sugano diagram (Scheme 2). Consequently, the spin–flip phosphorescence appears at low-energy (in the red to near-infrared domain) and the associated emission lifetimes reach a few milliseconds at low-temperature where vibrational quenching mechanisms are negligible. Whereas maximum ligand-field strengths have been early recognized as a crucial tool for inducing detectable phosphorescence in $Cr^{III}$ complexes,[24–26] the rational exploitation of the nephelauxetic effect for tuning the energy range of this delayed emission is more recent,[28,58,62–65,72] but it appears to be particularly promising as illustrated in Scheme 2. Replacing X = $CN^-$, with

X = $Cl^-$, $Br^-$ significantly reduces the energy gap $\Delta E = E(^4T_2) - E(^2T_1)$ from *ca.* 10 000 $cm^{-1}$ to 3000 $cm^{-1}$ (Table 2). This accelerates the quenching of the spin–flip emissive levels through back intersystem crossing (BISC) and the photoluminescence cannot be detected at room temperature for the heteroleptic halogenido complexes.

Although the heteroleptic $[Cr(\mathbf{L})(CN)_3]$ complexes match most of the structural and photophysical requirements for being exploited as building block in (supra)molecular assemblies containing compact $Ln^{III}$–X–$Cr^{III}$ light-converting units, their difficult synthesis and isolation combined with their low solubility and their sensitivity to thermally-activated emission quenching limit the perspectives for their use as sensitizers for molecular light upconversion. On the other side, the specific divergent meridional distribution of three CN– groups in the chromium complex might be cleverly exploited for designing d–f heterometallic magnetic materials according that some solid-state synthetic approaches could be developed.

## Experimental section

### General

Reagent grade acetonitrile (ACN) was distilled from $CaH_2$. *N,N*-Dimethylformamide was dried through an alumina cartridge. All other chemicals such as $CrBr_3{\cdot}6H_2O$, $AgCF_3SO_3$, 2,2′:6′,2″-terpyridine (tpy) and organic solvents were purchased from commercial suppliers and used without further purification. The ligand *N*,*N*′-dimethyl-*N*,*N*′-dipyridin-2-ylpyridine-2,6-diamine (ddpd),[69] 2,6-di(quinolin-8-yl)pyridine (dqp)[70] and the complexes $[Cr(tpy)Cl_3]$,[71] $[Cr(ddpd)Cl_3]$,[64] $[Cr(dqp)Cl_3]$[63] were prepared according to published methods. Silica-gel plates (Merck, 60 $F_{254}$) were used for thin-layer chromatography, SiliaFlash® silica gel P60 (0.04–0.063 mm), and Acros silica gel 60 (0.035–0.07 mm) were used for preparative column chromatography.

**Caution.** Cyanide waste solutions are harmful and toxic and must be carefully destroyed (see https://sensorex.com/blog/2016/04/26/cyanide-wastewater-treatment/). We systematically decontaminated all solutions or waste containing cyanide ions by treatment with 1 : 1 mixtures of sodium hypochlorite (35% in water) and sodium hydroxide (2 M in water).

### Preparation of $[Cr(tpy)Br_3]$[62]

2,2′:6′,2″-Terpyridine (tpy, 415 mg, 1.78 mmol) was dissolved in 50 mL of isopropanol. A solution of $CrBr_3{\cdot}6H_2O$ (708 mg, 1.77 mmol) in isopropanol (10 mL) was added dropwise and the resulting mixture was refluxed for 5 hours. The resulting green precipitate was filtered, washed with isopropanol (15 mL), hot ethanol (30 mL), dichloromethane (15 ml), diethylether (15 mL) and dried. Elemental analyses (Table S2†) were compatible with the formation of $[Cr(tpy)Br_3]$ (865 mg, 1.75 mmol, 93%) as a green powder. ESI-MS ($CH_3CN$) *m*/*z*: $[Cr(tpy)Br_2]^+$ calc.: 444.87, found: 444.7; $[Cr(tpy)Br]^+$ calc.: 363.95, found: 363.7. Small crystals suitable for XRD were obtained after a slow diffusion of $Et_2O$ into a solution of the complex in DMF.

### Preparation of $[Cr(ddpd)Br_3]$[62]

*N*,*N*′-Dimethyl-*N*,*N*′-dipyridin-2-ylpyridine-2,6-diamine (ddpd, 372 mg, 1.28 mmol) was dissolved in 50 mL of isopropanol. A solution of $CrBr_3{\cdot}6H_2O$ (489 mg, 1.22 mmol) in isopropanol (10 mL) was added dropwise and the resulting mixture was refluxed for 5 hours. The resulting green precipitate was filtered, washed with isopropanol (15 mL), hot ethanol (30 mL), dichloromethane (15 ml), diethylether (15 mL) and dried. Elemental analyses (Table S2†) were compatible with the formation of $[Cr(ddpd)Br_3]$ (534 mg, 0.92 mmol, 75%) as a green powder. ESI-MS ($CH_3CN$) *m*/*z*: $[Cr(ddpd)Br_2]^+$ calc.: 502.92, found: 502.5. Slow diffusion of diethyl ether into a concentrated solution of the complex in dimethylformamide led to the formation of green crystals suitable for X-ray diffraction.

### Preparation of $[Cr(dqp)Br_3]$

2,6-Di(quinolin-8-yl)pyridine (dqp, 167 mg, 0.50 mmol) and the $CrBr_3{\cdot}6H_2O$ (200 mg, 0.50 mmol) were charged in a vial with isopropanol (15 mL). The vial was sealed and heated in a microwave oven at 160° for 6 h. The solid was filtered and washed with isopropanol (15 mL), hot ethanol (30 mL), dichloromethane (15 mL), diethyl ether (15 mL) and dried. Elemental analyses (Table S2†) were compatible with the formation of $[Cr(dqp)Br_3]$ (236 mg, 0.38 mmol, 76% yield) as an olive green powder. ESI-MS ($CH_3CN$) *m*/*z*: $[Cr(dqp)Br_2]^+$ calc.: 544.90, found: 544.7.

### Preparation of $[Cr(tpy)(CN)_3]$

$AgCF_3SO_3$ (160 mg, 0.62 mmol) and $[Cr(tpy)Br_3]$ (103 mg, 0.20 mmol) were charged in a vial with dry acetonitrile (2 mL). The vial was sealed and the solution was heated in a microwave oven at 140 °C for 30 min. The white precipitate (AgBr) was separated by filtration and the clear orange red solution was used directly for the next step. ESI-MS ($CH_3CN$) *m*/*z*: $[Cr(tpy)(CF_3SO_3)_2]^+$ calc.: 582.94, found: 582.6, $[Cr(tpy)(CF_3SO_3)_3 + NH_4]^+$ calc.: 749.93, found: 750.0.

The solution of $[Cr(tpy)(CF_3SO_3)_3]$ was charged into a second vial containing a solution of KCN (43 mg, 0.66 mmol) partially dissolved in ethanol (5 mL). The sealed vial was heated in the microwave oven at 90 °C for 4 h. The resulting orange powder was filtered, and recrystallized from hot water to give $[Cr(tpy)(CN)_3]{\cdot}1.7H_2O$ (31 mg, $7.88 \times 10^{-5}$ mol, 39% yield). Small crystals suitable for XRD were obtained after recrystallization in hot water.

### Preparation of $[Cr(ddpd)(CN)_3]$

$AgCF_3SO_3$ (353 mg, 1.37 mmol) and $[Cr(ddpd)Br_3]$ (250 mg, 0.43 mmol) were charged in a vial with dry acetonitrile (5 mL). The vial was sealed and the solution was heated in a microwave oven at 140 °C for 30 min. The white precipitate (AgBr) was separated by filtration and the clear orange red solution was used directly for the next step. ESI-MS ($CH_3CN$) *m*/*z*: $[Cr(ddpd)(CF_3SO_3)_2]^+$ calc.: 640.99, found: 640.7.

 

The solution of $[Cr(ddpd)(CF_3SO_3)_3]$ was charged into a second vial containing a solution of KCN (95 mg, 1.47 mmol) partially dissolved in acetonitrile (5 mL). The sealed vial was heated in the microwave oven at 120 °C for 30 min. The resulting orange powder was filtered, then suspended in water to remove the $KCF_3SO_3$ and the excess of KCN. The solid was again filtered, washed with dichloromethane to remove the possible traces of free ddpd and dried to give $[Cr(ddpd)(CN)_3]\cdot 0.85H_2O\cdot 1.3CH_2Cl_2$ (135 mg, 0.25 mmol, 58% yield). Small crystals suitable for XRD were obtained after a slow evaporation of a solution of complex in a 1 : 1 acetone/water mixture.

### Preparation of $[Cr(dqp)(CN)_3]$

$AgCF_3SO_3$ (267 mg, 1.04 mmol) and $[Cr(dqp)Br_3]$ (201 mg, 0.32 mmol) were charged in a vial with dry acetonitrile (5 mL). The vial was sealed and the solution was heated in a microwave oven at 140 °C for 30 min. The white precipitate (AgBr) was separated by filtration and the clear orange red solution was used directly for the next step. ESI-MS ($CH_3CN$) *m*/*z*: $[Cr(dqp)(CF_3SO_3)_2]^+$ calc.: 682.97, found: 683.1.

The solution of $[Cr(dqp)(CF_3SO_3)_3]$ was charged into a second vial containing a solution of KCN (71 mg, 1.09 mmol) partially dissolved in acetonitrile (5 mL). The sealed vial was heated in the microwave oven at 90 °C for 1 h. The red/brown mixture was filtered to remove a brown solid. The red solution was evaporated under reduced pressure and a light red solid was obtained. The red solid was suspended in $H_2O$ to remove $KCF_3SO_3$ and the excess of KCN. The suspension was filtered and the red solid suspended in dichloromethane in order to remove the possible traces of free ligand. Final filtration and drying led to $[Cr(dqp)(CN)_3]\cdot 1.5H_2O\cdot 1.7CH_2Cl_2$ (51 mg, $8.03 \times 10^{-5}$ mol, 25% yield) as a red solid. Small crystals suitable for XRD were obtained by slow evaporation of a solution of complex in a 5 : 1 methanol/water mixture.

### Spectroscopic and analytical measurements

$^1H$ and $^{13}C$ NMR spectra were recorded at 298 K on a Bruker Avance 400 MHz spectrometer. Chemical shifts are given in ppm with respect to TMS. Pneumatically-assisted electrospray (ESI-MS) mass spectra were recorded from $\sim 1 \times 10^{-4}$ M (ligands) and $\sim 1 \times 10^{-3}$ M (complexes) solutions on an Applied Biosystems API 150EX LC/MS System equipped with a Turbo Ionspray source. Elemental analyses were performed by K. L. Paglia using a Microchemical Laboratory of the University of Geneva (Switzerland). FT-IR spectra were recorded with a Bruker Tensor 27 spectrometer equipped with a platinum ATR. Electronic spectra in the UV-Vis region were recorded at 293 K from $CH_3CN$ solutions with a PerkinElmer Lambda 1050 using quartz cells of 0.1 or 1.0 mm path length. Solid-state diffuse reflectance spectra were recorded using UV/Vis/NIR PerkinElmer Lambda 900 in reflectance (*R*) mode fitted with an integrating sphere. The pure samples were placed between two 1.0 mm path length quartz cells whose background cell was filled with pure MgO. The signal of pure MgO was used as the baseline. Emission spectra (excitation at 355 nm) and excitation spectra were recorded from frozen solution samples at 77 K ($c \approx 2 \times 10^{-5}$ mol $L^{-1}$) or from acetonitrile solution ($c \approx 2 \times 10^{-5}$ mol $L^{-1}$) at 293 K, with a Fluorolog (Horiba Jobin–Yvon), equipped with iHR320, a Xenon lamp 450 Watt Illuminator (FL-1039A/40A) and a water-cooled photo multiplier tube (PMT Hamamatsu R2658 or R928), and corrected for the spectral response of the system. For time-resolved experiments, the decay curves were recorded at 77 K and 293 K, using a photomultiplier (Hamamatsu R2658 or R928) and a digital oscilloscope (Tektronix MDO4104C). Pulsed excitation at 355 nm was obtained with the third harmonic of a pulsed Nd:YAG laser (Quantel Qsmart850) or by a pulsed diode light source NanoLED 375L (<200 ps pulse, HORIBA Scientific). Low temperature (77 K) was achieved using liquid quartz transparent Dewar filled with liquid $N_2$ in the center of which samples were placed. Acetonitrile/propionitrile or DMF solutions ($c \approx 2 \times 10^{-5}$ mol $L^{-1}$) were introduced in quartz tube (4 mm interior diameter) introduced in sample holder of the Dewar. The oxygen free decay curve measurements were done at 293 K on acetonitrile or DMF solutions of the complex. The complexes in quartz tube were dissolved in acetonitrile or DMF then degassed by freeze pump thaw, and filled with argon. Aerated solutions were prepared by using no-degassed acetonitrile or DMF as solvent. Quantum yields were calculated using $[Cr(ddpd)_2]^{3+}$ as reference ($\lambda_{exc}$ = 435 nm; Q.Y. = 12.1% in $CH_3CN$).[58]

### X-ray crystallography

Summary of crystal data, intensity measurements and structure refinements for complexes $[Cr(tpy)Br_3]$, $[Cr(tpy)(CN)_3]$, $[Cr(ddpd)(CN)_3]\cdot 2H_2O$ and $[Cr(dqp)(CN)_3]\cdot 3.28H_2O$ were collected in Tables S3, S6, S9 and S12.† Pertinent bond lengths, bond angles and interplanar angles were collected in Tables S4, S5, S7, S8, S10, S11, S13 and S14† together with ORTEP views, pertinent numbering schemes and intermolecular interactions gathered in Fig. S2–S11.† The crystals were mounted on Hampton cryoloops with protection oil. X-ray data collections were performed with an XtaLAB Synergy-S diffractometer equipped with an hybrid pixel hypix arc 150 detector. The structures were solved by using dual space methods.[83] Full-matrix least-square refinements on $F^2$ were performed with SHELXL.[84] within the OLEX2 refinement package.[85] CCDC 2133575–2133578† contain the supplementary crystallographic data.

### Theoretical calculations

The Gaussian 16 software package was used to perform structural optimizations of the investigated complexes. Starting from the X-ray diffraction structures, the ground state, $^4A_2$, structures of the different complexes were obtained from DFT optimizations using the unrestricted version of the Becke three-parameters exchange function in combination with the Lee–Yang–Parr correlation functional (UB3LYP). The basis set used for these optimizations was the 6-31G(d,p) for N, C and H and the LanL2DZ for the metal center. In addition, LANL2 pseudopotential was specified for the core electrons of

the Cr atom. Solvent effects were included *via* the Polarizable Contiunuum Model (PCM) as implemented in Gaussian 16 with the dielectric constant of *N,N*-dimethylformamide (for $[Cr(tpy)(CN)_3]$) and acetonitrile (for $[Cr(ddpd)(CN)_3]$ and $[Cr(dqp)(CN)_3]$). Optimized geometries were confirmed to be stationary points by analysis of their vibrational frequencies. Orbital and spin density information was extracted from the optimized geometries. The 50 lowest energetic transitions were calculated by TD-DFT, using the unrestricted version of the Coulomb-attenuated B3LYP functional (UCAM-B3LYP), selecting the 6-31++G(d,p) basis set for N, C and H, and the LanL2DZ for the metal center. Same pseudopotential for the Cr atom and solvent effects were selected as for the ground state calculations. Electron Density Difference Maps (EDDM) were computed using GaussSum 3.0[86] and are represented with an isoval = 0.002 using GaussView 6.1.1.[87]

## Conflicts of interest

There are no conflicts to declare.

## Acknowledgements

Financial support from the Swiss National Science Foundation is gratefully acknowledged (grant numbers: 200020_178758 and 206021_183324). Carlos M. Cruz thankfully acknowledge Prof. Dr Michal Juríček for his support and access to the UZH Service and Support for Science IT ($S^3IT$) computing facilities.

## References

1 J. Ribas Gispert, *Coordination Chemistry*, Wiley-VCH Verlag, Weinheim, 2008, pp. 228–233.
2 J.-R. Jiménez, B. Doistau, M. Poncet and C. Piguet, *Coord. Chem. Rev.*, 2021, **434**, 213750.
3 R. Lescouëzec, L. M. Toma, J. Vaissermann, M. Verdaguer, F. S. Delgado, C. Ruiz-Perez, F. Lloret and M. Julve, *Coord. Chem. Rev.*, 2005, **249**, 2691–2729.
4 M. Verdaguer, A. Bleuzen, V. Marvaud, J. Vaissermann, M. Seuleiman, C. Desplanches, A. Scuiller, C. Train, R. Garde, G. Gelly, C. Lomenech, I. Rosenman, P. Veillet, C. Cartier and F. Villain, *Coord. Chem. Rev.*, 1999, **190**, 1023–1047.
5 W. Dong, L. N. Zhu, H. B. Song, D. Z. Liao, Z. H. Jiang, S. P. Yan, P. Cheng and S. Gao, *Inorg. Chem.*, 2004, **43**, 2465–2467.
6 C. K. Jorgensen, *Adv. Chem. Phys.*, 1963, **5**, 33–146.
7 *Multiplets of Transition-Metal Ions in Crystals, Pure and Applied Physics*, ed. S. Sugano, Y. Tanabe and H. Kamimura, 1970, 33, pp. 1–333.
8 J. Ferguson, *Prog. Inorg. Chem.*, 1970, **12**, 159–293.
9 H. Witzke, *Theor. Chim. Acta*, 1971, **20**, 171–185.
10 A. B. P. Lever, *Inorganic Electronic Spectroscopy*, Elsevier, Amsterdam-Oxford-New York-Tokyo, 1984, pp. 417–429.
11 A. Hauser and C. Reber, *Struct. Bonding*, 2017, **172**, 291–312.
12 S. Adachi, *J. Lumin.*, 2021, **232**, 117844.
13 M. G. Brik and C.-G. Ma, *Theoretical Spectroscopy of Transition Metal and Rare Earth Ions*, Jenny Stanford Publishing, Singapore, 2020, pp 298–304.
14 J. M. Herrera, A. Bachschmidt, F. Villain, A. Bleuzen, V. Marvaud, W. Wernsdorfer and M. Verdaguer, *Philos. Trans. R. Soc., A*, 2008, **366**, 127–138.
15 J. Dreiser, K. S. Pedersen, C. Piamonteze, S. Rusponi, Z. Salman, M. Ali, E. M. Schau-Magnussen, C. A. Thuese, S. Piligkos, H. Weihe, H. Mutka, O. Waldmann, P. Oppeneer, J. Bendix, F. Nolting and H. Brune, *Chem. Sci.*, 2012, **3**, 1024–1032.
16 E. J. L. McInnes, G. A. Timco, G. F. S. Whitehead and R. E. P. Winpenny, *Angew. Chem., Int. Ed.*, 2015, **54**, 14244–14269.
17 S. K. Langley, D. P. Wielechowski, B. Moubaraki and K. S. Murray, *Chem. Commun.*, 2016, **52**, 10976–10979.
18 M. Darawsheh, L. A. Barrios, O. Roubeau, S. J. Teat and G. Aromi, *Angew. Chem., Int. Ed.*, 2018, **57**, 13509–13513.
19 C. Pichon, N. Suaud, C. Duhayon, N. Guihery and J. P. Sutter, *J. Am. Chem. Soc.*, 2018, **140**, 7698–7704.
20 F.-F. Chen, Z.-Q. Chen, Z.-Q. Bian and C.-H. Huang, *Coord. Chem. Rev.*, 2010, **254**, 991–1010.
21 L. Aboshyan-Sorgho, M. Cantuel, S. Petoud, A. Hauser and C. Piguet, *Coord. Chem. Rev.*, 2012, **256**, 1644–1663.
22 P. S. Wagenknecht, N. A. P. Kane-Maguire, D. G. Speece and N. Helwic, *Inorg. Chem.*, 2002, **41**(5), 1229–1235.
23 A. Cadranel, P. S. Oviedo, P. Alborés, L. M. Baraldo, D. M. Guldi and J. H. Hodak, *Inorg. Chem.*, 2018, **57**(6), 3042–3053.
24 L. S. Forster, *Chem. Rev.*, 1990, **90**, 331–353.
25 A. D. Kirk, *Chem. Rev.*, 1999, **99**, 1607–1640.
26 P. S. Wagenknecht and P. C. Ford, *Coord. Chem. Rev.*, 2011, **255**, 591–616.
27 O. S. Wenger, *J. Am. Chem. Soc.*, 2018, **140**, 13522–13533.
28 C. Forster and K. Heinze, *Chem. Soc. Rev.*, 2020, **49**, 1057–1070.
29 P. A. Scattergood, *Organomet. Chem.*, 2021, **43**, 1–34.
30 N. A. P. Kane-Maguire, *Top. Curr. Chem.*, 2007, **280**, 37–67.
31 L. S. Forster, *Coord. Chem. Rev.*, 2006, **250**, 2023–2033.
32 P. A. Brayshaw, J.-C. G. Bünzli, P. Froidevaux, J. M. Harrowfield, Y. Kim and A. N. Sobolev, *Inorg. Chem.*, 1995, **34**, 2068–2076.
33 T. Lazarides, G. M. Davies, H. Adams, C. Sabatini, F. Barigelletti, A. Barbieri, S. J. A. Pope, S. Faulkner and M. D. Ward, *Photochem. Photobiol. Sci.*, 2007, **6**, 1152–1157.
34 L. Aboshyan-Sorgho, H. Nozary, A. Aebischer, J.-C. G. Bünzli, P.-Y. Morgantini, K. R. Kittilstved, A. Hauser, S. V. Eliseeva, S. Petoud and C. Piguet, *J. Am. Chem. Soc.*, 2012, **134**, 12675–12684.
35 L. A. Büldt and O. S. Wenger, *Chem. Sci.*, 2017, **8**, 7359–7367.
36 L. Aboshyan-Sorgho, C. Besnard, P. Pattison, K. R. Kittilstved, A. Aebischer, J.-C. G. Bünzli, A. Hauser and C. Piguet, *Angew. Chem., Int. Ed.*, 2011, **50**, 4108–4112.

 

37 Y. Suffren, D. Zare, S. V. Eliseeva, L. Guénée, H. Nozary, T. Lathion, L. Aboshyan-Sorgho, S. Petoud, A. Hauser and C. Piguet, *J. Phys. Chem. C*, 2013, **117**, 26957–26963.
38 B. Golesorkhi, H. Nozary, A. Fürstenberg and C. Piguet, *Mater. Horiz.*, 2020, **7**, 1279–1296.
39 J. Kalmbach, C. Wang, Y. You, C. Forster, H. Schubert, K. Heinze, U. Resch-Genger and M. Seitz, *Angew. Chem., Int. Ed.*, 2020, **39**, 18804–18808.
40 S. M. Stevenson, M. P. Shores and E. M. Ferreira, *Angew. Chem., Int. Ed.*, 2015, **54**, 6506–6510.
41 R. F. Higgins, S. M. Fatur, S. G. Shepard, S. M. Stevenson, D. J. Boston, E. M. Ferreira, N. H. Damrauer, A. K. Rappe and M. P. Shores, *J. Am. Chem. Soc.*, 2016, **138**, 5451–5464.
42 S. Otto, A. M. Nauth, E. Emilov, N. Scholz, A. Friedrich, U. Resch-Genger, S. Lochbrunner, T. Opatz and K. Heinze, *ChemPhotoChem*, 2017, **1**, 344–349.
43 M. D. Ward, *Coord. Chem. Rev.*, 2010, **254**, 2634–2642.
44 W. R. Browne, N. m. O'Boyle, J. J. McGarvey and J. G. Vos, *Chem. Soc. Rev.*, 2005, **34**, 641–663.
45 D. L. Dexter, *J. Chem. Phys.*, 1953, **21**, 836.
46 P. A. Tanner, *Coord. Chem. Rev.*, 2010, **254**, 3026–3029.
47 X.-Y. Wang, R. R. Valiev, T. Y. Ohulchanskyy, H. Agren, C. Yang and G. Chen, *Chem. Soc. Rev.*, 2017, **46**, 4150–4167.
48 P. A. Tanner, L. Zhou, C. Duan and K.-L. Wong, *Chem. Soc. Rev.*, 2018, **47**, 5234–5265.
49 Z. Q. You, C. P. Hsu and G. R. Fleming, *J. Chem. Phys.*, 2006, **124**, 044506.
50 A. Ghaith, L. S. Forster and J. V. Rund, *Inorg. Chim. Acta*, 1986, **116**, 11–13.
51 C. K. Ryu, R. B. Lessard, D. Lynch and J. F. Endicott, *J. Phys. Chem.*, 1989, **93**, 1752–1759.
52 C. Wegeberg and O. S. Wenger, *Dalton Trans.*, 2022, **51**, 1297–1302.
53 C. Wegeberg and O. S. Wenger, *JACS Au*, 2021, **1**, 1860–1876.
54 P. Herr, C. Kerzig, C. B. Larsen, D. Häussinger and O. S. Wenger, *Nat. Chem.*, 2021, **13**, 956–962.
55 J. B. Bilger, C. Kerzig, C. B. Larsen and O. S. Wenger, *J. Am. Chem. Soc.*, 2021, **143**, 1651–1663.
56 S. Otto, M. Grabolle, C. Förtser, C. Kreitner, U. Resh-Genger and K. Heinze, *Angew. Chem., Int. Ed.*, 2015, **54**, 11572–11576.
57 S. Otto, M. Dorn, C. Förster, M. Bauer, M. Seitz and K. Heinze, *Coord. Chem. Rev.*, 2018, **359**, 102–111.
58 J. R. Jimenez, B. Doistau, C. M. Cruz, C. Besnard, J. M. Cuerva, A. G. Campana and C. Piguet, *J. Am. Chem. Soc.*, 2019, **141**, 13244–13252.
59 E. C. Constable, C. E. Housecroft, M. Neuburger, J. Schönle and J. A. Zampese, *Dalton Trans.*, 2014, **43**, 7227–7235.
60 J. Schönle, E. C. Constable, C. E. Housecroft, M. Neuburger and J. A. Zampese, *Inorg. Chem. Commun.*, 2015, **51**, 75–77.
61 J. Schönle, E. C. Constable, C. E. Housecroft, A. Prescimone and J. A. Zampese, *Polyhedron*, 2015, **89**, 182–188.
62 J.-R. Jiménez, B. Doistau, C. Besnard and C. Piguet, *Chem. Commun.*, 2018, **54**, 13228–13231.
63 J.-R. Jiménez, M. Poncet, B. Doistau, C. Besnard and C. Piguet, *Dalton Trans.*, 2020, **49**, 13528–13532.
64 D. Zare, B. Doistau, H. Nozary, C. Besnard, L. Guénée, Y. Suffren, A.-L. Pelé, A. Hauser and C. Piguet, *Dalton Trans.*, 2017, **46**, 8992–9009.
65 B. Doistau, J.-R. Jiménez, S. Guerra, C. Besnard and C. Piguet, *Inorg. Chem.*, 2020, **59**, 1424–1435.
66 K. D. Barker, K. A. Barnett, S. M. Connel, J. W. Glaeser, A. J. Wallace, J. Wildsmith, B. J. Herbert, J. F. Wheeler and N. A. P. Kane-Maguire, *Inorg. Chim. Acta*, 2001, **316**, 41–49.
67 E. G. Donnay, J. P. Schaeper, R. D. Brooksbank, J. L. Fox, R. G. Potts, R. M. Davidsdon, J. F. Wheeler and N. A. P. Kane-Maguire, *Inorg. Chim. Acta*, 2007, **360**, 3272–3280.
68 D. C. Luehrs, R. T. Iwamoto and J. Kleinberg, *Inorg. Chem.*, 1966, **5**, 201–204.
69 A. Breivogel, C. Forster and K. Heinze, *Inorg. Chem.*, 2010, **49**, 7052–7056.
70 M. Jaeger, L. Eriksson, J. Bergquist and O. Johansson, *J. Org. Chem.*, 2007, **72**, 10227–10230.
71 N. Cloete, H. G. Visser and A. Roodt, *Acta Crystallogr., Sect. E: Struct. Rep. Online*, 2007, **63**, M45–M47.
72 N. Sinha, J.-R. Jiménez, B. Pfund, A. Prescimone, C. Piguet and O. S. Wenger, *Angew. Chem., Int. Ed.*, 2021, **60**, 23722–23728.
73 S. Jagner, E. Ljungstrom and N. G. Vannerberg, *Acta Chem. Scand.*, 1974, **A28**, 623–630.
74 C. E. Housecroft and A. G. Sharpe, *Inorganic Chemistry*, Pearson Education Limited, England, 4th edn, 2021, p. 82.
75 K. Nakamoto, Infrared and Raman Spectra of Inorganic and Coordination Compounds. Part B: Applicaton in Coordination, in *Organometallic and Bioinorganic Chemistry*, John Wiley & Sons, Inc., New York-Chichester-Weinheim-Brisbane-Singapore-Toronto, 1997, pp. 105–113.
76 L. H. Jones, *Inorg. Chem.*, 1963, **2**, 777–780.
77 D. L. Wood, J. Ferguson, K. Knox and J. F. Dillon, *J. Chem. Phys.*, 1963, **39**, 890–898.
78 S. Otto, N. Scholz, T. Behnke, U. Resh-Genger and K. Heinze, *Chem. – Eur. J.*, 2017, **23**, 12131–12135.
79 J. J. Alexander and H. B. Gray, *J. Am. Chem. Soc.*, 1968, **90**, 4260–4271.
80 J. Maillard, K. Klehs, C. Rumble, E. Vauthey, M. Heilemann and A. Fürstenberg, *Chem. Sci.*, 2021, **12**, 1352–1362.
81 J. Maillard, C. A. Rumble and A. Fürstenberg, *J. Phys. Chem. B*, 2021, **125**, 9727–9737.
82 C. Forster, M. Dorn, T. Reuter, S. Otto, G. Davarci, T. Reich, L. Carrella, E. Rentschler and K. Heinze, *Inorganics*, 2018, **6**, 86.
83 G. M. Sheldrick, *Acta Crystallogr., Sect. A: Found. Adv.*, 2015, **71**, 3–8.
84 G. M. Sheldrick, *Acta Crystallogr., Sect. C: Struct. Chem.*, 2015, **71**, 3–8.
85 O. V. Dolomanov, L. J. Bourhis, R. J. Gildea, J. A. K. Howard and H. Puschmann, *J. Appl. Crystallogr.*, 2009, **42**, 339–341.
86 N. M. O'Boyle, A. L. Tenderholt and K. M. Langner, *J. Comput. Chem.*, 2008, **29**, 839–845.
87 R. Dennington, T. A. Keith and J. M. Millam, *GaussView, Version 6.1.1*, Semichem Inc., Shawnee Mission, KS, 2016.